# Evaluation of fringe effect of electrical resistance tomography sensor

Jiangtao Sun[*] and Wuqiang Yang

School of Electrical and Electronic Engineering, The University of Manchester, Manchester M13 9PL, UK

_____

## Highlights

• We have evaluated the fringe effect of an single-plane ERT sensor with different axially non-homogeneous object distributions.

• A compensation method for the fringe effect has been proposed.

• Experiment was carried out to validate the findings from simulation and the effectiveness of the compensation method.

_____

Abstract

A conventional electrical resistance tomography (ERT) sensor uses pin electrodes for current injection, and the electric field spreads far beyond the electrode plane, as a result of "soft field" nature. This phenomenon is referred to as "fringe effect" and would cause measurement errors and image distortion. The impact of fringe effect on measurement and reconstructed images depends on the object distributions, the conductivity contrast and others. It is not trivial to evaluate the fringe effect of an ERT sensor and its impact on the measurement and the reconstructed images. In this paper the fringe effect of an ERT sensor is evaluated for central core and off-central core distributions at different axial positions and with different axial dimensions and conductivity contrasts. Then, how to compensate for the fringe effect of the ERT sensor is discussed and a method proposed for improving the measurement accuracy and image reconstruction. Finally, the findings and methodology is verified by experiment.

## 1. Introduction

Electrical resistance tomography (ERT), often referred to as electrical impedance tomography (EIT), has been developed since 1980's. Its applications have been extended from medical imaging to industrial monitoring and measurement, e.g. multi-phase flows with conductive medium inside cylindrical pipes or vessels. To measure a multi-phase flow, 2D or 3D images may be reconstructed. While some researchers worked on 3D image reconstruction, realistically, 2D image reconstruction is preferred because it is much simpler and faster than 3D image reconstruction. To obtain a 2D image for a cylindrical pipe or vessel, a certain number of electrodes (say 16) are normally mounted evenly around its inner surface to form a single-plane ERT sensor. To obtain 3D images, a multi-plane ERT sensor, i.e. multiple single-plane ERT sensors at different axial layers, is needed. While the current-injection and voltage-measurement strategy is usually adopted for ERT measurement, different protocols can be applied for data acquisition, e.g. adjacent, opposite and diagonal with non-conductive boundary for 2D ERT imaging (Dickin and Wang, 1996). Among those protocols, the adjacent strategy is the most popular and used for data acquisition in this paper.

Since the material distribution of a multi-phase flow in industry and the electric field of an Electrical Tomography (ET) sensor are essentially 3D, a great effort has been dedicated to 3D imaging with ERT and electrical capacitance tomography (ECT) (Banasiak *et al*, 2010; Banasiak *et al*, 2012; Cao and Xu, 2013; Dehghani *et al*, 2005; Li, 2008; Marashdeh *et al*, 2008; Murphy *et*

_____

[*] Corresponding author. Tel.: +44-0161-306-4792.
E-mail: jiangtao.sun@postgrad.manchester.ac.uk  (JT Sun)

*al*, 2006; Pinheiro *et al*, 1998; Soleimani *et al*, 2007; Soleimani *et al*, 2009; Warsito and Fan, 2005; Wilkinson *et al*, 2006). Even though the achieved 3D imaging results seem promising, more effort is needed to improve the image quality. Firstly, most of them are implemented with incomplete measurement data because the electrodes on both the bottom and top sides of the true 3D sensor are normally removed for flow measurement (Soleimani *et al*, 2007). The one with complete measurement data should be similar to true 3D ECT imaging proposed by Li (2008) and Soleimani *et al* (2007). It means that they are only approximated 3D imaging. Secondly, the condition number of the sensitivity matrix of a 3D ET sensor is much larger than that of a 2D sensor due to the increased number of unknowns, as compared by Li (2008) between 2D and true 3D ECT sensors. A much larger condition number means that 3D ET imaging presents a more severely ill-posed and ill-conditioned problem and would be tolerant to very small errors caused by the measurement noises or simulation errors (Soleimani *et al*, 2007). This brings high demands on sensor fabrication and measurement electronics. A fast reconstruction algorithm was implemented by Pinheiro *et al* (1998) to reduce the condition number of 3D ERT imaging but led to deteriorated image resolution. Thirdly, 3D imaging with a reasonable resolution takes a much longer time than 2D imaging (Li, 2008; Pinheiro *et al*, 1998; Soleimani *et al*, 2007) because it normally needs to obtain the approximated inverse of a very large sensitivity matrix for image reconstruction, as indicated by the large number of independent measurements and voxels for imaging. This would limit its application in situations with high commands on the real-time performance. Even though 3D imaging by a single-plane ET sensor was attempted, either the position or the shape of the object cannot be correctly reconstructed (Cao and Xu, 2013; Soleimani *et al*, 2007). More geometry parameters in a 3D ET sensor also makes the sensor design more difficult than a 2D ET sensor since the approximated 3D imaging is an "open-field" as described by Li (2008). In view of the above points, 2D ET imaging is preferred in most cases.

As discussed by Sun and Yang (2013), the fringe effect would occur with 2D ET imaging because certain conditions should be satisfied to make it permissible that the 3D reconstruction can be simplified to 2D with tolerate errors. The first condition is that the electric field should be confined inside an ERT sensor and axially homogeneous. This can guarantee a 3D electric field to be represented by the corresponding 2D one. The second one is that the material distribution should be axially homogeneous. This would guarantee the 3D material distribution to be simplified into a 2D distribution. If any one of those two conditions is not satisfied, severe fringe effect may occur.

Up to now the fringe effect of ERT sensors for 2D imaging has not been investigated systematically. The fringe effect was illustrated qualitatively and avoided by using voltage excitation and long strip electrodes (not pin electrodes) as described by Li and Yang (2009). It was investigated quantitatively by comparing the simulation results of a 3D ERT sensor with the corresponding 2D analysis when the fringe effect was ignored (Ma *et al*, 1997), or with the corresponding experimental results (Fransolet *et al*, 2002). However, the comparison was made quantitatively only for simulated or measured potential differences before normalization, which may be referred to as "absolute" fringe effect. The image-forming mechanism of an EIT system was described by using equi-current perturbation hypothesis and axially extending an object from the sensor plane to a distant position, aiming at investigating the fringe effect with different electrode pairs (Rabbani and Kabir, 1991). It was concluded that where the disturbed equi-current surface with the largest current density intersects the cross-section of the EIT sensor is where the largest change in the reconstructed image would take place. The image reconstructed for the extended objects covering the whole cross section would be circular, but for the extended objects not covering the whole cross section, the situation would be more complicated. Wang (1999) also conducted research into the fringe effect in EIT with experimental, simulation and analytical models. One of the findings was that the axial 3D attenuation range (3/4 attenuation) regarding the EIT sensor plane would be one third of the vessel's diameter. Another phenomenon discovered was that the image reconstructed for a small object in the halfway between the center and the pipe wall and moving away from the sensor plane would move towards the center of the sensor cross section. But these two findings did not account for the influences of the object length on the fringe effect since only a small non-conductive ball was taken as a test object in the experiment. Sun and Yang (2013) found that similar fringe effect exists in ECT and ERT sensors if both of them are excited by a voltage signal, and increasing the electrode length and grounded end guards would reduce the fringe effect in both cases. But the fringe effect of the conventional ERT sensors with the current injection strategy was not investigated, e.g. the normalized potential differences or resistance. Therefore, it is worthwhile evaluating the fringe effect of single-plane ERT sensors with the current injection strategy, especially with the normalized measurements, which are actually used for image reconstruction.

ERT may be applied to various industrial processes, e.g. multi-phase flow imaging and measurement, which normally involves a conductive fluid as the continuous phase and non-conductive material as the dispersed phase, e.g. in a bubble column (Fransolet *et al*, 2001; Fransolet *et al*, 2005; Toye *et al*, 2005; Jin *et al*, 2007; Vijayan *et al*, 2007). The dispersed phase is usually measured and imaged, with the distribution being axially non-homogeneous. In this case there would exist severe fringe effect. This brings the necessity to study the fringe effect with axially non-homogeneous distribution. Because of many possible distributions, a specified ERT sensor with a typical distribution, i.e. core distribution, is investigated, aiming to compensate the fringe effect in 2D imaging. This involves examining whether the above two conditions are satisfied with different measurement strategies, evaluating how large the fringe effect is with objects of different lengths and conductivities and what the influence is when the objects are placed at different axial and cross-sectional positions. Thus a method is proposed on the basis of phenomenon discovered during future investigations to compensate for the fringe effect of the ERT sensor in different situations. Experimental verification of the findings and the proposed methodology is then presented.

## 2. Image reconstruction and ERT sensor

### 2.1. Linear Back Projection (LBP) and Evaluation

Before numerical simulation, it is necessary to introduce a popular image reconstruction algorithm, linear back-projection (LBP). It is a simple single step method, which is used for both ERT and ECT. Two crucial aspects in LBP for ERT need to be considered: the sensitivity maps and the normalised resistance. The element in a 2D sensitivity map, e.g. the sensitivity of electrode pairs $i - j$ ($i$ for excitation and $j$ for measurement) to the conductivity change in a pixel at position $(x, y)$ with an area of $P(x, y)$, is defined as (Dickin and Wang, 1996; Lionheart, 2001):

$$S_{i,j}(x, y) = \int_{P(x,y)} \frac{E_i(x, y)}{I_i} \cdot \frac{E_j(x, y)}{I_j} dx\, dy \qquad (1)$$

where $E_i(x, y)$ and $E_j(x, y)$ are the electric field strength at $(x, y)$ when the $i_{th}$ and $j_{th}$ electrode pairs are injected with currents $I_i$ and $I_j$ respectively in turn.

The normalized resistance is defined as (Dickin and Wang, 1996; Giguère *et al*, 2008):

$$\lambda(i, j) = \frac{V_m(i, j) - V_r(i, j)}{V_r(i, j)} \qquad (2)$$

where $\lambda(i, j)$ is the normalized change in the potential difference for the measurement electrode pair $j$ with the injection electrode pair $i$, $V_m(i, j)$ and $V_r(i, j)$ are the measured and reference potential differences for the measurement electrode pair $j$ with the injection electrode pair $i$ respectively. The reference voltage difference is acquired when the sensor is filled with conductive background medium.

The LBP algorithm is expressed as (Yang and Peng, 2003):

$$g = \frac{S^T \lambda}{S^T \mu_\lambda} \qquad (3)$$

where $g$ is the normalized conductivity vector, $S$ is the sensitivity matrix of the ERT sensor, $S^T$ is the transpose of $S$, $\lambda$ is the normalised resistance vector, and $\mu_\lambda$ is the identity vector, i.e. $\mu_\lambda = [1,1,1,...,1]$.

$S$ can be calculated by Eq. 1, element by element and electrode pair by electrode pair, and $\lambda$ can be obtained by Eq. 2. Note that the sensitivity maps are for 2D. To evaluate the image quality, the relative image error and correlation coefficient can be calculated as in Eq. 4 and Eq. 5 respectively (Yang and Peng, 2003) with respect to the corresponding reconstructed image from 2D simulation model. These two indexes will be used in this paper to evaluate the fringe effect induced by objects inside the sensor.

$$RIE = \frac{\|\hat{g} - g\|}{\|g\|} \qquad (4)$$

$$CC = \frac{\sum_{i=1}^{N}(\hat{g}_i - \bar{\hat{g}})(g_i - \bar{g})}{\sqrt{\sum_{i=1}^{N}(\hat{g}_i - \bar{\hat{g}})^2 \sum_{i=1}^{N}(g_i - \bar{g})^2}} \qquad (5)$$

Where $RIE$ is the relative image error, $CC$ is the correlation coefficient, $g$ is the reference conductivity distribution (the corresponding reconstructed image for 2D simulation model in this paper), $\hat{g}$ is the reconstructed conductivity distribution for an object inside the sensor plane, $\bar{\hat{g}}$ and $\bar{g}$ are the mean values of $g$ and $\hat{g}$ respectively.

To evaluate the fringe effect induced by objects outside the sensor, the norm ratio may be used and formulated as:

$$NR = \frac{\|\hat{g}\|}{\|g\|} \qquad (6)$$

Where $NR$ is the norm ratio of two images, $\hat{g}$ is the reconstructed conductivity distribution for an object outside the sensor plane, and $g$ is the reconstructed conductivity distribution for 2D simulation model.

### 2.2. Simulation Model for ERT Sensor

It was believed that an ECT sensor with long electrodes would have less fringe effect with axially homogeneous distributions, so that the 3D distribution can be simplified into 2D, because of smaller differences between the normalised capacitance from 3D

and 2D simulations. Whether this is true for ERT sensors is discussed in this section. A simulation model for an ERT sensor is established. A single-plane ERT sensor is shown in Fig. 1 with its geometry parameters and material properties listed.
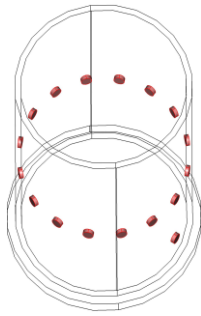


Fig. 1. Simulation model of an ERT sensor

- Diameter of electrode: 9 mm
- Inner Diameter:14.1 cm
- Bottom diameter: 16.5 cm
- Gap between bottom and electrode plane: 10 cm
- Number of electrodes per electrode plane: 16
- Material of tube: Perspex
- Material of electrodes: Steel
- Gap between the unused electrode and sensor plane: 6 cm
- Height of the tube: 21 cm
- Depth of saline: 19.8 cm

The real ERT sensor used for experimental verification has five electrode planes, but only the middle one was used in the simulation as a single-plane ERT sensor as shown in Fig. 1. In the 3D simulation, the ERT sensor is filled with saline as the background medium (the upper boundary for FEM simualtion is above the middle cross-section of the electrode plane by 10 cm while the lower boundary is below the middle cross-section of the electrode plane by 9.8 cm). The unused electrode below the sensor plane in Fig. 1 is grounded in the simulation to assemble the real situation in practical ERT measurements for the reduction of common mode signals. Note that saline with conductivity of 0.02 S/m was used as the background medium inside the ERT sensor in all the following 3D and 2D simulation. The 2D model of the one plane ERT sensor with the object distribution is shown in Fig. 2:



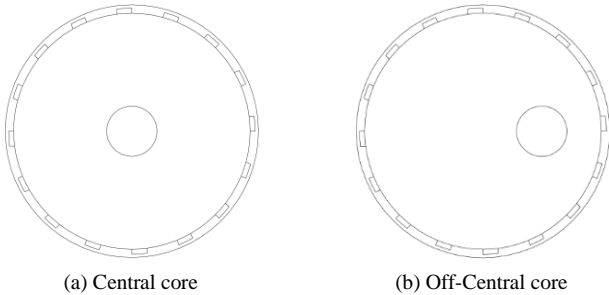(a) Central core          (b) Off-Central core

Fig. 2. 2D model of the single-plane ERT sensor with object distribution

The cross-sectional object distribution for evaluation of fringe effect is shown in Fig. 2, with a cylindrical rod of 3 cm in diameter in the center or off-central midway. It is used as the reference distribution in the following 3D simulation while the rods are variable in axial length and position for different purposes. The 2D ERT sensor in Fig. 2 (a) or (b) will also be used in all the following 2D simulation to obtain sensitivity maps and corresponding 2D results. Note that all the simulation was carried out in COMSOL Multiphysics with the "In-Plane Electric Currents" mode in the 2D case and "Electric Currents" mode in the 3D case, both of which are in AC/DC module with 10 kHz as the excitation frequency. In the 3D simulation, tetrahedral elements and direct solver (SPOOLES) are used. To ensure the numerical accuracy (i.e. the difference in normalized resistance between a coarse mesh and a finer one is below 2%), the mesh density is increased until the simulated resistance after normalization converges. The number of elements used in the simulation is of the order of 90,000. Taking the ERT sensor shown in Fig. 1 as an example to show the influence of mesh size on simulation, the first coarse mesh (the used one) consists of 88,314 tetrahedral elements, and a finer one consists of 180,527 elements, which are shown in Fig. 3 (a) and (b) respectively.

The simulated potential differences before normalization (i.e. the tube is filled with homogeneous background medium) and after normalization (with an axially homogeneous object distribution as shown in Fig. 2(a)) with these two meshes are shown in Fig. 4, which shows the 13 values when an adjacent electrode pair is injected with current in each case. They have the maximum difference of 1.4% with these two meshes in both cases. This partially verifies the numerical accuracy of the 3D simulation with the specified mesh. Note that all simulation was done on a PC with an Intel CoreTM i7-2600 3.4 GHz CPU, 64-bit Windows7 and 8 GB memory. Also note that the contact impedance is not included in all the ERT sensors to isolate the fring effect from other error sources and also because the contact impedance in an industrial application can be ignored with the current injection strategy and a measurement circuit of high input impedance (Szczepanik and Rucki, 2007).
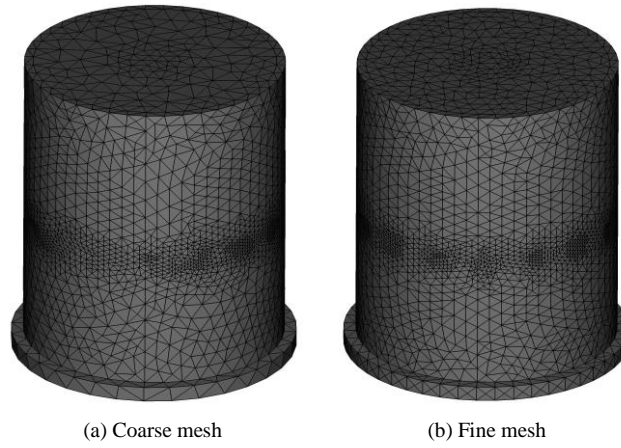
(a) Coarse mesh        (b) Fine mesh

Fig. 3. Meshes



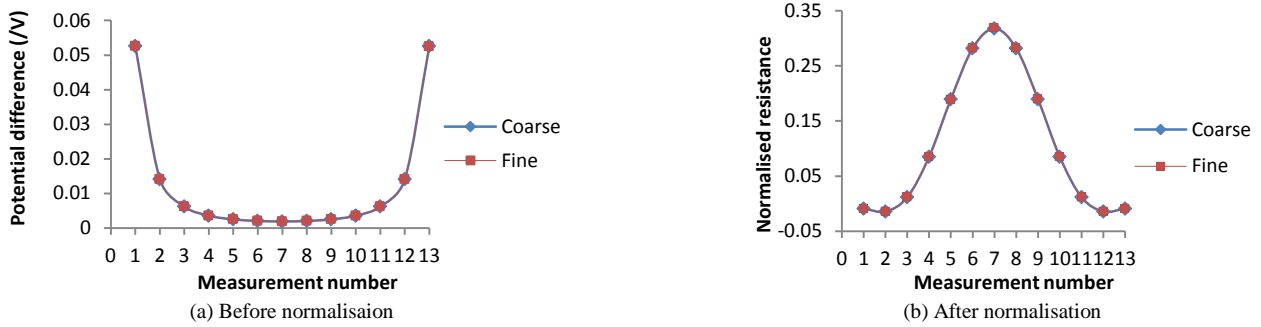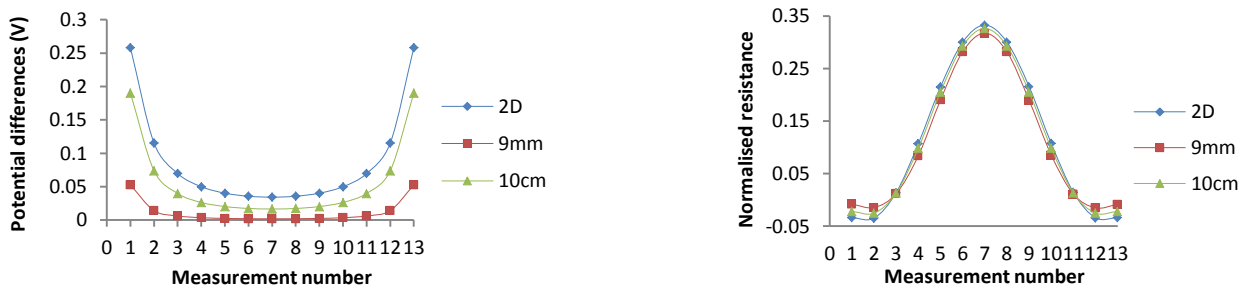(a) Before normalisaion        (b) After normalisation

Fig. 4. Comparison between the simulated potential difference before and after normalization with different meshes

### 2.3. Difference between ECT and ERT measurement models

A 2D and two 3D ERT sensors are considered in this subsection. The 2D and the first 3D model are the same as shown in Fig. 2 and Fig. 1, respectively. The second 3D model was built by changing the small round electrodes of the first 3D model to be rectangle electrodes of 10 cm in length and the same width and axial position with other geometry parameters unchanged. To investigate the fringe effect with axially homogeneous distribution, the ERT sensors, no matter 2D or 3D, were first filled with the background medium, i.e. saline with conductivity of 0.02 S/m. Currents were injected into the three sensors with the same density per cm$^2$. The simulated potential differences for those three models are shown in Fig. 5 (a) when an adjacent electrode pair is injected with current.

Fig. 5 (a) shows that there is a very large difference between the simulated potential differences in the 2D and 3D ERT sensors with 9 mm long electrodes. This difference may be referred to as "absolute" fringe effect, which would be eliminated with infinitely long electrodes as in an ECT sensor. However, it is the normalized resistance that accounts in ERT. An axially homogeneous distribution as discussed previously was set up with a non-conductive rod of the same length as the tube depth (19.8 cm) intruding into the background medium along the middle axis of the tube with both the 2D and 3D sensors. The resultant normalized resistance is shown in Fig. 5 (b). Note that all the objects inside the sensor in all the following 3D simulation and experiments were placed axially symmetric to the sensor plane unless specified.

Fig. 5. Comparison between simulated potential differences before and after normalization for the 2D and 3D ERT sensors with two different electrode lengths

Unlike the potential differences in Fig. 5 (a), Fig. 5 (b) shows very small difference between simulated normalized resistance for the 2D ERT sensor and the 3D ERT sensors. It seems that the normalization process for ERT could reduce the fringe effect greatly. However, this does not agree with the corresponding conclusion with ECT sensors (Sun and Yang, 2013). A possible reason is that ECT adopts the voltage excitation strategy while ERT normally adopts the current injection strategy. The former can be referred to as "Low Z measurement" while the latter as "High Z measurement". The equivalent circuits in these two cases have been discussed in (Neumayer $et$ $al$, 2011). For the former there is a single coupling capacitance between the excitation and detection electrodes and for the latter there is actually a voltage divider involving all the impedances between possible electrode pairs. With the adjacent current injection and voltage measurement strategy, the detailed equivalent circuit for ERT measurement can be found in (Szczepanik and Rucki, 2007) and is shown in Fig. 6, which is for 2D case only. In Fig. 6 (b), $Z_H$, $Z_L$, $Z_{V_1}$ and $Z_{V_2}$ are the contact or electrochemical impedances at the injecting electrodes $H$ and $L$ and the measuring electrodes $V_1$ and $V_2$, respectively. The former two have no influence on the potential difference measurement while the latter two are negligible for a measurement circuit with high input impedance. $R_{H_1}$ to $R_{H_n}$ and $R_{L_1}$ to $R_{L_n}$ represent the resistance between the equi-potential line $V_1$ and the injecting electrode $H$ and between the equi-potential line $V_2$ and the injecting electrode $L$, respectively, which also do not affect the potential difference measurement. $R_1$ to $R_n$ are the resistances to be measured.



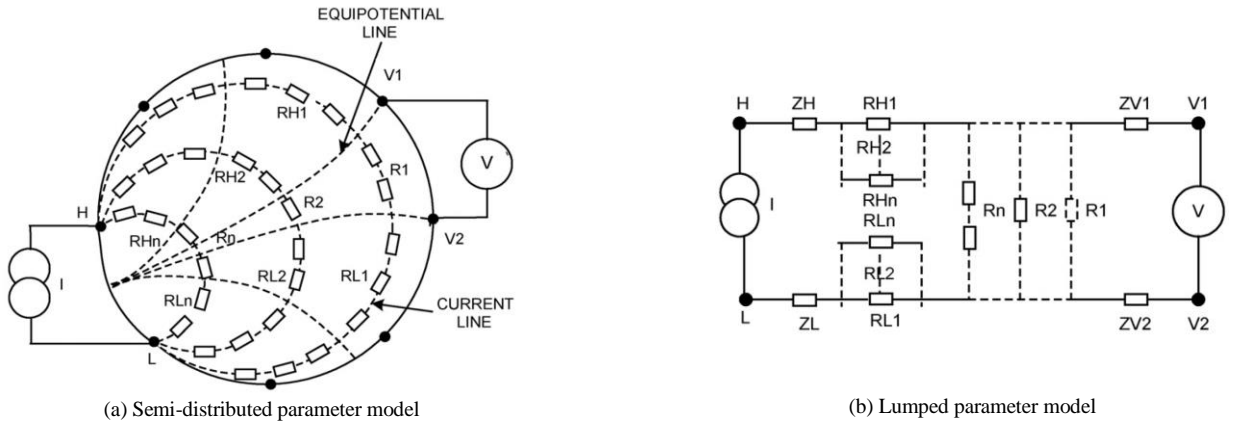(a) Semi-distributed parameter model    (b) Lumped parameter model

Fig. 6. Electrical model of the ERT sensor proposed by Szczepanik and Rucki (2007)

In the 3D case with fringe effect, the equivalent circuit of an ERT sensor would be more complicated with each defined axial layer similar to the 2D case. If only a single resistance is used to denote the parallel summation of $R_1$ to $R_n$ as shown in Fig. 6 (b) in each defined axial layer, then the 3D equivalent circuit of ERT would be as shown in Fig. 7 (b). The same for the 3D equivalent circuit of ECT is shown in Fig. 7 (a).
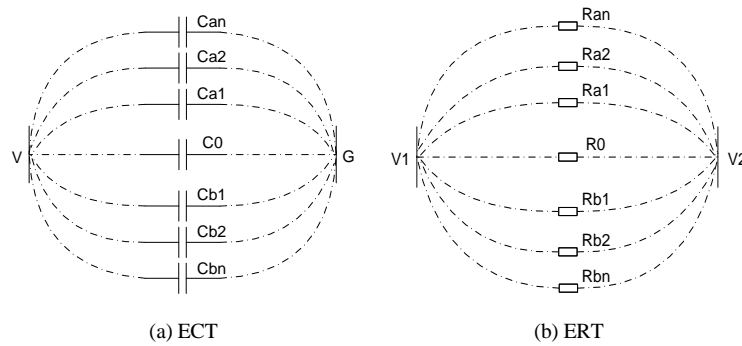


(a) ECT    (b) ERT

Fig. 7. 3D models for ECT and ERT measurement

In Fig. 7 (a), $C_0$ stands for the elementary capacitance between the excitation electrode $V$ and the detection electrode $G$, i.e. without the fringe effect. $C_{a_1}$ to $C_{a_n}$ and $C_{b_1}$ to $C_{b_n}$ denote the capacitance induced by the fringe effect above and below the ECT sensor plane, respectively. Similarly in Fig. 7 (b), $R_0$ stands for the elementary resistance between detection electrodes $V_1$ and $V_2$ without the fringe effect. $R_{a_1}$ to $R_{a_n}$ and $R_{b_1}$ to $R_{b_n}$ represent the resistance induced by the fringe effect above and below the ERT

sensor plane, respectively. Fig. 7 shows that the 3D equivalent circuits for ECT or ERT are a series of capacitors or resistors in parallel along the axial direction, respectively. For ECT, the equivalent capacitance of the circuit in Fig. 7 (a) can be expressed as:

$$C_{equ} = C_{a_1} + C_{a_2} + \cdots + C_{a_n} + C_0 + C_{b_1} + C_{b_2} + \cdots + C_{b_n} \quad (7)$$

For ERT, the equivalent resistance in Fig. 7 (b) can be expressed as:

$$R_{equ} = R_{a_1} // R_{a_2} // \cdots // R_{a_n} // R_0 // R_{b_1} // R_{b_2} // \cdots // R_{b_n} \quad (8)$$

With an axially homogeneous distribution, the largest coupling capacitance in Fig. 7 (a) is the one inside the ECT sensor plane ($C_0$), while the smallest resistance in Fig. 7 (b) is the one inside the ERT sensor plane ($R_0$). The other coupling capacitance or resistance would attenuate or increase with their distance from the electrode plane for axially homogeneous distribution. The larger the coupling capacitance or the smaller the resistance when the tube is filled with a homogeneous background medium, the more impact the permittivity or conductivity change in the corresponding axial layer would have on the related measurement. For an ECT sensor with enough long electrodes, say the same as or larger than the sensor diameter, the largest capacitance in Fig. 7 (a) would be much larger than other capacitance which would dominate the equivalent capacitance $C_{equ}$ in Eq. 7, i.e. most electric field lines would be confined inside or within certain small axial range above and below the ECT sensor plane. This means the fringe effect is negligible since the electric field distribution is approaching to the 2D case. But this is not the case with much shorter electrodes than the sensor diameter. This is why the fringe effect of ECT sensors would become less and less with the increase in the electrode length. For an ERT sensor with the adjacent current injection, however, the situation would be very different. As shown in Fig. 6 (b), the measured resistance in the 2D case is a parallel summation of resistance between the two equi-potential lines defined by the two measurement electrodes. Since those two equi-potential lines both origin from somewhere between the two current injection electrodes as shown in Fig. 6 (a), the resistance between them and near the current injection electrodes, like $R_n$, is much smaller than others even with very short electrodes (e.g. 9 mm as in Fig. 1), which would dominate the equivalent resistance $R_{equ}$ in Eq. 8, i.e. most current would flow inside or within certain small axial range above and below the ERT sensor plane. This means negligible fringe effect occurs in this case since the current distribution is approaching to the 2D case. With longer electrodes, only a little improvement can be achieved due to the very small distance between the current injection electrodes, which may indicate that the electrical field of an ERT sensor with the adjacent strategy is more focused than that of an ECT sensor in terms of normalised measurements. This is why the conventional ERT sensor as shown in Fig. 1 has negligible fringe effect with the adjacent strategy in terms of the normalised resistance.

A direct proof for the above explanation is that different levels of fringe effect exist for an ECT sensor with certain length but different distribution. Normally, the adjacent electrode pairs with axially homogeneous distribution near the pipe wall have less fringe effect than the opposite ones with axially homogeneous distribution along the middle axis of the sensor (Sun and Yang, 2013), because the largest elementary capacitance normally exists between adjacent electrode pairs, while the smallest one between the opposite ones. To further verify this, the opposite strategy was used for current injection and voltage measurement with the above two ERT sensors (of 9 mm and 10 cm long electrodes repecitvely), where the resistance between the two defined equi-potential lines and near the current injection electrodes is not as small as with the adjacent strategy. The normalised resistance with the opposite strategy for the above 2D and 3D ERT sensors with the specified axially homogeneous distribution is shown in Fig. 8. Note that only 6 out of the 7 normalised resistance values are shown in Fig. 8 because the eliminated voltage measurement is nearly zero with the opposite strategy and induces very large errors after normalisation. Unlike in Fig. 5 (b), Fig. 8 shows that the normalised resistance for the 3D ERT sensor with electrodes of 10 cm is much closer to the 2D one, i.e. much less fringe effect. This validates the above explanation.
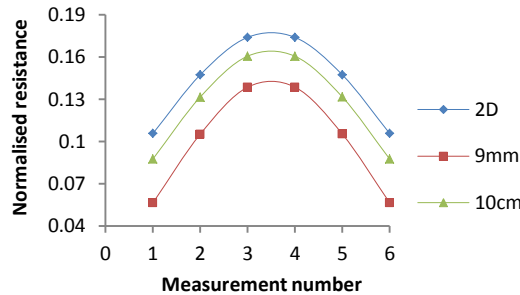


Fig. 8. Normalized resistance for 2D and 3D ERT sensors with different electrode lengths and homogeneous distribution using opposite strategy

The above discussion shows that there is negligible fringe effect for a conventional ERT sensor with very short electrodes and the specified axially homogeneous distribution with the adjacent strategy. However, the situation would be different with axially non-homogeneous distribution. A simple non-homogeneous distribution would be a non-conductive cylindrical rod shorter than the tube in length intruding into the background medium along the tube axis. In this case, some resistance inside the layers without the rod similar to those in Fig. 7 (b) would be reduced compared with the previous case. This would result in the reduction of the equivalent resistance in Eq. 8, causing the normalised resistance to decrease due to the unchanged reference, i.e. more severe fringe effect in this case. To evaluate the fringe effect with non-conductive rods of different lengths and at different axial positions, 3D simulation was carried out and the corresponding results are presented and discussed in the following sections.

## 3. Fringe effect of ERT sensor with non-axially homogeneous distributions
### 3.1. Centred non-conductive or conductive perterbation inside the sensor plane

In the first set of simulations, the distribution investigated is that with centered non-conductive or conductive objects, the same as in Fig. 2 (a). They are positioned inside and axially symmetrically against the electrode plane with the 3D model in Fig. 1, i.e. core distribution. Because the tube in Fig. 1 has a limited length of 19.8 cm, the length of the centered rod is set to be 1, 4, 7, 10 and 19.8 cm respectively in the simulation to evaluate the fringe effect. The normalized resistance in these situations is shown in Fig. 9 (a), (b) and (c) with the corresponding 2D result as the reference. Note that for comparison, the conductivity of the conductive rods was set to be 0.06 S/m and 2 S/m, which are identified by the captions "Conductive" and "Highly conductive" respectively in Fig. 9.
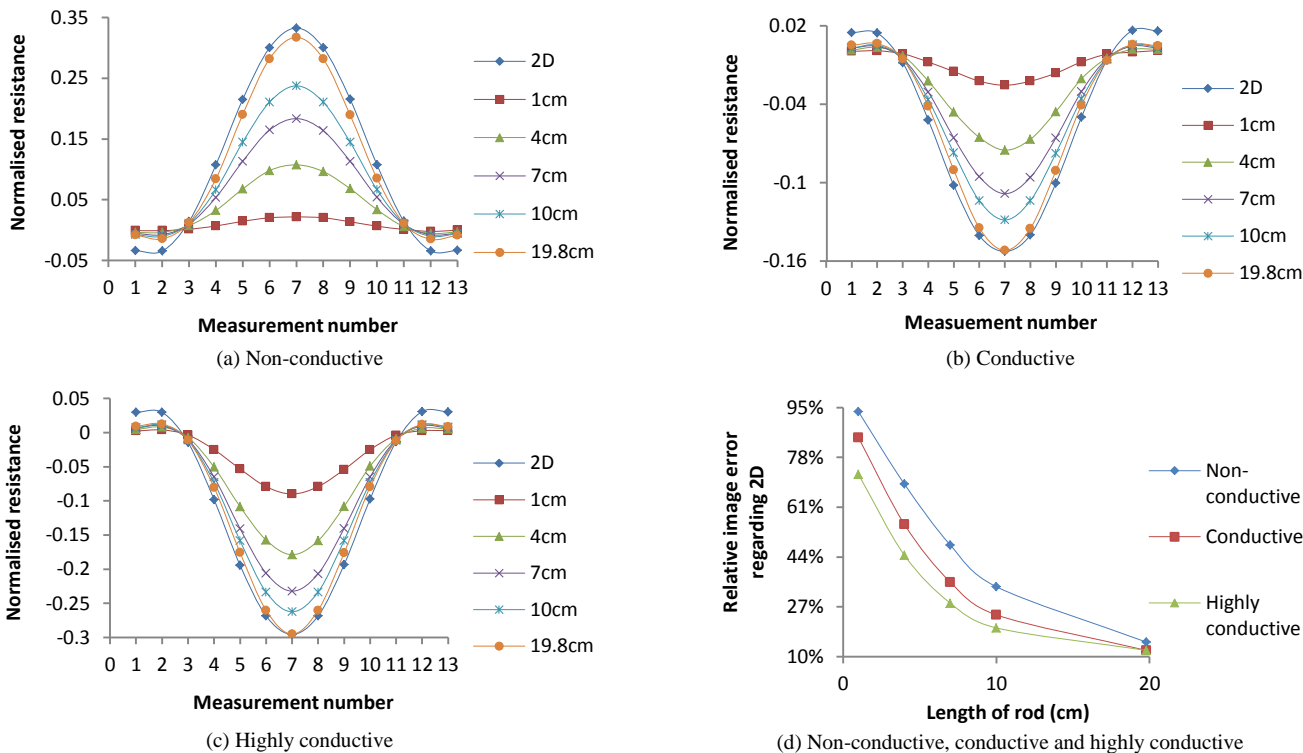


Fig. 9. Normalized resistance (a-c) and relative image errors of reconstructions regarding 2D one (d) for non-conductive, conductive and highly conductive object inside the sensor and with different lengths

Fig. 9 (a) (b) and (c) show that the longer the centered rod, the more similar the normalized resistance to the 2D reference, i.e. longer object gives less fringe effect. To quantify the fringe effect with the above core distribution, images were reconstructed based on their normalized resistance using LBP and the sensitivity maps from the 2D model as shown in Fig. 2. To evaluate the image error induced by the fringe effect, the image with the corresponding 2D model in Fig. 9 is used as reference and the relative image errors of reconstructions for the 3D models are calculated as in Eq. 4 and shown in Fig. 9 (d). It shows that the relative image errors for the centered core distribution decrease with the increase in the object length in each case. This means that the fringe effect is reduced when longer object emerges inside and along the middle axis of the ERT sensor. This can be explained by the fact that the object distribution would become more and more homogeneous along the axial direction with the increase in the object

length. This would eventually enable the permissibility of the 3D object distribution and electric field being represented by the corresponding 2D ones with tolerate errors.

Fig. 9 (d) shows that less fringe effect occurs with the highly conductive object, especially when the object length is very short, because the highly conductive object part within the sensor plane would reduce the elementary resistance $R_0$ in Fig. 7 (b) and attract more current to itself, compared with non-conductive or less conductive object, which would result in the reduction of fringe effect. To illustrate how the fringe effect affects the reconstructed image, the reconstruction results corresponding to the results in Fig. 9 (a) (for centered non-conductive objects) are shown in Fig. 10. In Fig. 10, the reconstructed images are very dim when the rod is very short, e.g. 1 cm and 4 cm long, and become more and more similar to the 2D result when the rod length increases. The reconstruction results for centered conductive objects are similar to those in Fig. 10.

Since the variation of fringe effect with the length of the conductive object along the middle axis of the sensor is similar to that of the corresponding non-conductive object, the following sections will only discuss the fringe effect for the latter, which is also the most common in ERT. It is found that longer electrodes in an ECT sensor would induce less fringe effect for axially homogeneous distribution. For non-homogeneous distribution, especially with a small object simulated above, however, long electrodes would average the effect of the object as indicated by the definition of capacitance. This makes the sensitivity decrease or fringe effect increase. Similarly, an ERT sensor with long electrodes (like 10 cm) would further average the response of non-axially homogeneous object, i.e. the response would be smaller than the above result for each object length. This would result in more severe fringe effect. Therefore, short electrodes are preferred for small object. Therefore, this paper mainly discusses the fringe effect of an ERT sensor with small size or "pin" electrodes, i.e. the conventional ERT sensor as shown in Fig. 1.

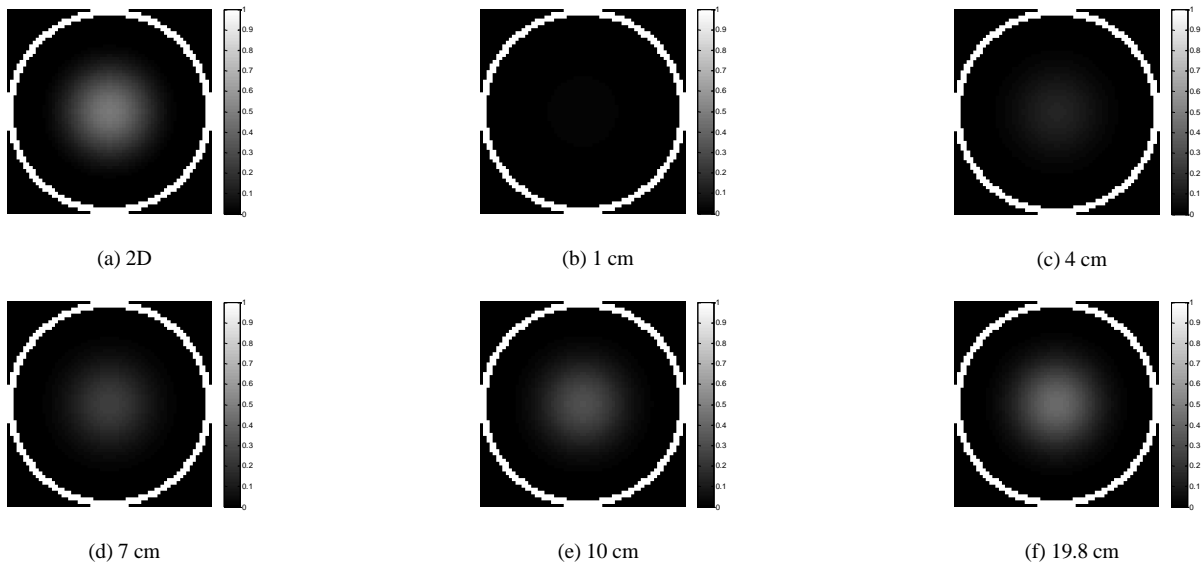|         |         |         |
|---------|---------|---------|
| (a) 2D  | (b) 1 cm | (c) 4 cm |
| (d) 7 cm | (e) 10 cm | (f) 19.8 cm |

Fig. 10. Reconstruction results for core distribution inside the sensor and with different lengths

## 3.2. Centred non-conductive perterbation outside the sensor plane

This section will investigate the fringe effect with centered non-conductive objects outside the sensor plane, which should not be sensed and reconstructed by an ERT sensor. However, the object would appear in the reconstructed images as artifacts due to the fringe effect. In the second set of simulations, centered non-conductive objects are positioned above the sensor plane by 0 cm, 1 cm and 3 cm along the middle axis of the sensor. Their lengths are set according to the length of the tube part above the sensor plane. The normalized resistance for the object distribution is shown in Fig. 11 (a), (b) and (c).

Fig. 11 (a), (b) and (c) show that long object outside the electrode plane can still have significant influence on the normalised resistance if the object is very close to the sensor plane. This is due to the existence of severe fringe effect in this case. This kind of influence is undesirable and should be eliminated to obtain high axial resolution and measurement accuracy. To quantify how significant this kind of influence is for objects with the specified lengths, images are reconstructed based on the normalised resistance and using LBP and the sensitivity maps from the 2D model. The norm ratios of the reconstructed images for those 3D objects to that for the 2D model are calculated as in Eq. 6 and shown in Fig. 11 (d). Note that this kind of norm ratio is not the relative image error since images for these objects are taken as undesirable artefacts.

Fig. 11 (d) shows that the norm ratios increase with the increase in the object length when the object is placed above the sensor plane by certain distance. The norm ratio can reach 33.64% for the object of length 10 cm above the sensor plane by 0 cm, which is a significant error. However, it would attenuate with the axial distance of the object from the sensor plane for each

specified length as shown in Fig. 9 (d). It is less than 12% with 7 cm long object above the sensor plane by 3 cm. Further simulation shows that it is less than 5% when a similar object with a length of 5 cm (the farthest from the sensor plane) is placed above the sensor plane by 5 cm. A similar conclusion was drawn by Wang (1999) that the 3D attenuation range (3/4 attenuation) in the axial direction regarding the electrode plane is one third of the vessel's diameter (around 4.7 cm) with a non-conductive ball of small dimensions in the half-way between the pipe wall and the centre. In principle, the attenuation of the fring effect is due to the attenuation of the electric field strength or the equivalent resistance along the axial direction of the sensor, as concluded from the previous 3D model for ERT.
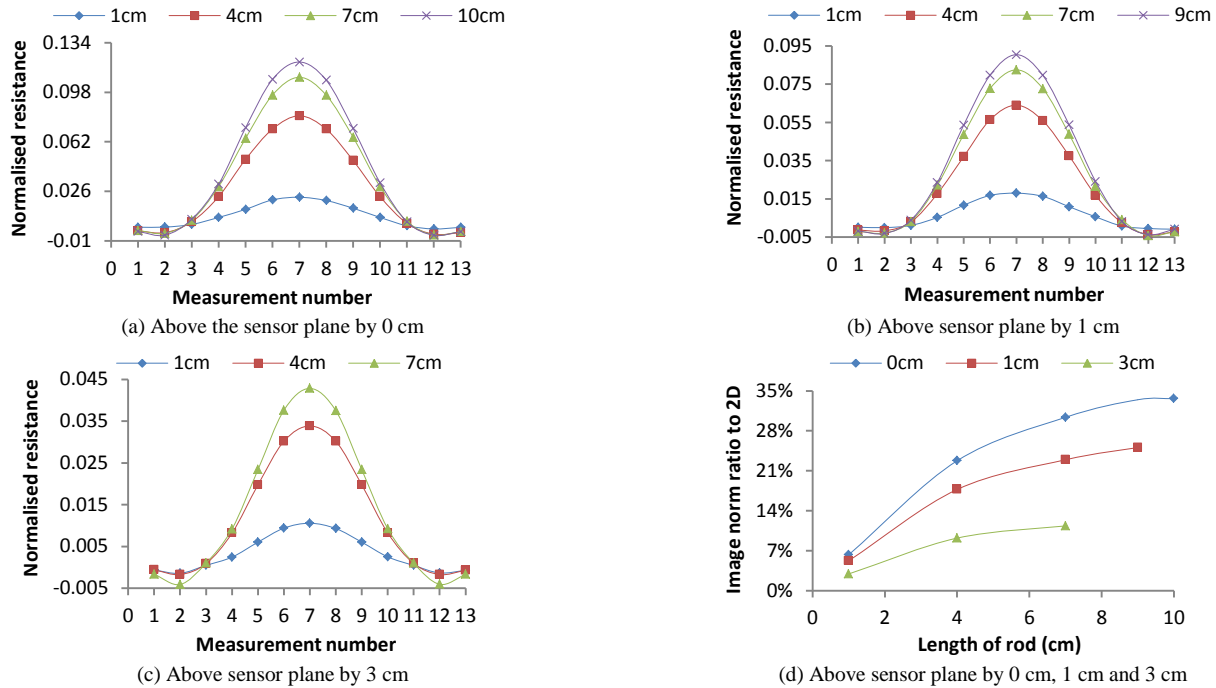


Fig. 11. Normalized resistance (a-c) and norm ratios of reconstructed images to 2D reference (d) for non-conductive object above the sensor plane by 0 cm, 1 cm and 3 cm with different lengths

The above simulation results for non-conductive object outside the sensor plane indicate that the further away the object from the electrode plane, the less impact it would have on ERT measurement, i.e. less fringe effect. This agrees with the deductions made from the 3D circuit model for ERT that the smaller the resistance in each axial layer when the tube is filled with a homogeneous background medium, the more impact its change would have on ERT after introducing an object.

3.3.  Noncentred non-conductive perterbation inside or outside the sensor plane

The previous sections discussed about the fringe effect for a centred object with different lengths and conductivity inside or outside the sensor plane. For generality, it is needed to investigate the fringe effect with a non-centred cylindrical object inside or outside the sensor plane. In the third and fourth sets of simulations, non-conductive objects with the same diameter as in the previous simulation were simulated for this purpose. The position of these objects in the cross section is shown in Fig. 2 (b), which is nearly half-way between the center and the tube wall. In the third sets of simulations, objects are placed inside the sensor plane and their axial lengths are set to be 1, 10 and 19.8 cm for comparison. The simulated resistance after normalisation is shown in Fig. 12 (a) together with the 2D reference.

Fig. 12 (a) shows that the fringe effect decreases with the object length. Certain fringe effect still exists when the object length is the longest (19.8 cm), which is also the case for the centered object, because the electric field cannot be completely confined within the ERT sensor plane and would be axially non-uniform even with this axially homogeneous object. It shows that the fringe effect in this case would change with the relative position of the injection and measurement electrode pairs to the object. The closer the injection electrode pair to the object and the larger part of the object lies between the two equi-potential lines defined by the measurement electrode pair as shown in Fig. 6 (a), the more severe fringe effect would be in the corresponding normalised resistance. This may be explained by the fact that the small distance between the injection electrode pair and the non-conductive object would make the small equivalent resistance near the injection electrode pair, e.g. $R_n$ in Fig. 6 (a), increase greatly, if most part of the object lie between the corresponding equi-potential lines. This would increase the elementary

resistance of corresponding measurement electrode pair, i.e. $R_0$ in Fig. 7 (b), and some resistance induced by the fringe effect above or below the sensor plane would be comparable with it. This would result in more current flowing outside and further away from the sensor plane, i.e. more severe fringe effect. If the injection electrode pair is far away from the object or the resistance of the measurement electrode pair is only slightly affected, only a slightly more current would flow outside, which means less fringe effect.

As mentioned in Introduction, Wang (1999) found that the image reconstructed for a small object in the half-way between the center and pipe wall and axially moving away from the sensor plane would move towards the center of the sensor cross section. This means that the artifacts produced by this kind of object may influence the reconstructed image near the center of the sensor. To investigate this phenomenon, objects are placed above the sensor plane by 0, 3 and 5 cm in the fourth sets of simulations and all set to be 4 cm in length. Their normalized resistance from simulation is shown in Fig. 12 (b).
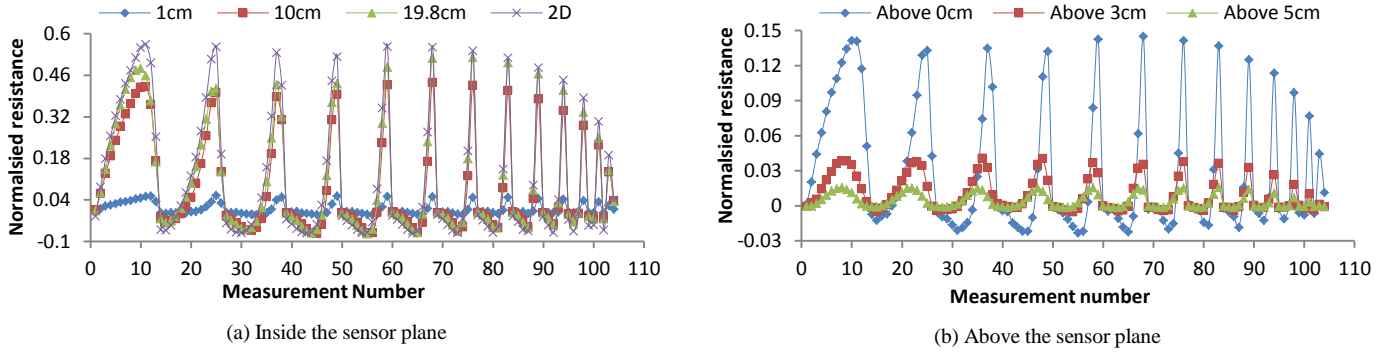


Fig. 12. Normalized resistance for non-centered non-conductive object inside or above the sensor plane by different distance

Fig. 12 (b) shows that with a fixed length, the further the object away from the electrode plane, the less fringe effect. This is consistent with the conclusion made from the previous simulation results. However, it is observed that the curve of the normalized resistance against the measurement number changes with the distance of the object from the sensor plane. With the distance of 0 cm, the shape of the curve is similar to that with the object inside the sensor plane as shown in Fig. 12 (a). The further the object away from the sensor plane, the more similar the shape is to that with the centered non-conductive object inside the sensor as shown in Fig. 9 (a), especially with the distance of 5 cm as shown in Fig. 12 (b). This means the reconstructed 2D image for the object would approach to the center of the cross section with their axial distance from the sensor plane, which confirms the conclusion made by Wang (1999). However, the fringe effect would decrease rapidly with the increase in the distance of the object from the sensor plane, as indicated by the normalized resistance for the objects above the sensor plane by 0, 3 and 5 cm in Fig. 12 (b). This makes it possible to reduce the fringe effect by compensation, which will be discussed in the next section.

3.4. Compensation for fringe effect in ERT sensor

To reduce the fringe effect in ERT sensors, there are two possible ways: incorporating guard electrodes to the sensor structure, e.g. driven or grounded end guards, or using a compensation algorithm during image reconstruction. Since driven guards are proven to be ineffective on reducing the fringe effect of ERT sensors (Wang, 1999) and the grounded end guards cannot be applied in ERT sensors with the current-injection and voltage-measurement strategy (Sun and Yang, 2013), a possible compensation method is discussed in this section.

The previous simulation results, e.g. Fig. 9 (a) and Fig. 12 (a), show that it is possible to reduce the fringe effect by scaling the corresponding normalized resistance for non-conductive object of certain length inside the sensor, because those resultant curves of the normalized resistance have similar shape but different magnitudes, except for those with axially homogeneous distribution. In this case, there is much less fringe effect. However, this is unlikely to happen in reality. For the object outside the sensor, they normally have less influence on the normalized resistance, compared with those with the same lengths but inside the sensor. Therefore, it is possible to reduce this kind of fringe effect by removing the resultant signals contained in the normalized resistance. To achieve both the above goals, selective scaling is a possible solution, to amplify signals after removing the small signal induced by fringe effect. Note that the selective scaling is not necessary when the object is inside the sensor plane. For example, the normalized resistance for object of 1 cm and 10 cm used in Fig. 9 (a) and Fig. 12 (a) can be scaled directly by assigning the scaling factor with the ratio of the maximum normalized resistance values in the 2D and corresponding 3D cases. The results after scaling are shown in Fig. 13. It shows that the fringe effect would be reduced after scaling the normalized resistance accordingly. Reconstruction results reveal that the relative image errors (calculated according to Eq. 4) after scaling is around 11% for both centered object in Fig. 13 (a), while the correlation coefficient (calculated according to Eq. 5) reaches 99.9% in both cases. Compared with the corresponding results in Fig. 9 (d), the relative image errors have been greatly reduced with negligible image distortion (indicated by the large correlation coefficients) after scaling. With the non-centered object, the relative image errors

corresponding to the normalized resistance of 1 and 10 cm object in Fig. 12 (a) is 91.4% and 30.8% respectively. After scaling, they are reduced to 36.4% and 15.3% respectively with correlation coefficients 91.5% and 98.8%, which means the image distortion is still negligible in both cases. The reconstructed images for these central and off-central core distributions are shown in Fig. 14 with the corresponding 2D results as the reference.
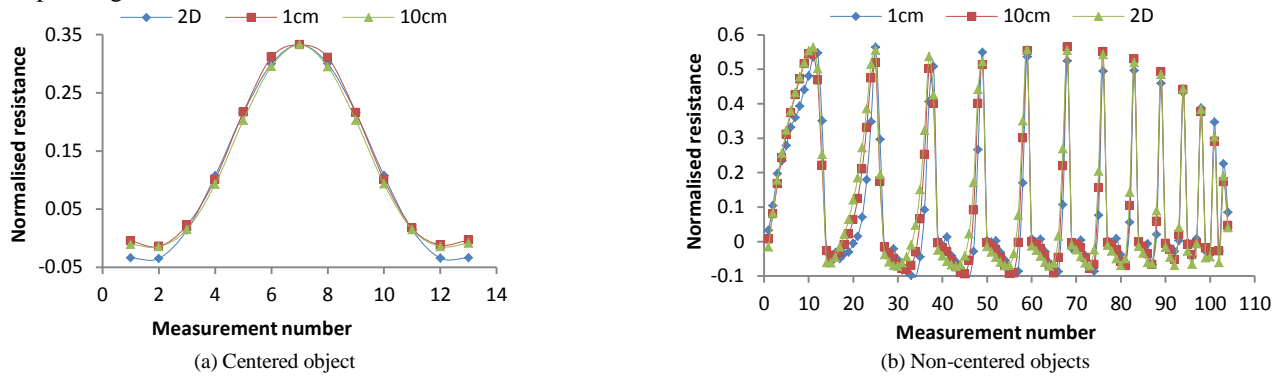


(a) Centered object



(b) Non-centered objects

Fig. 13. Normalized resistance after scaling for centered or non-centered non-conductive object inside the sensor



(a) 2D (central)



(b) 1 cm (central)



(c) 10 cm (central)



(d) 2D (off-central)



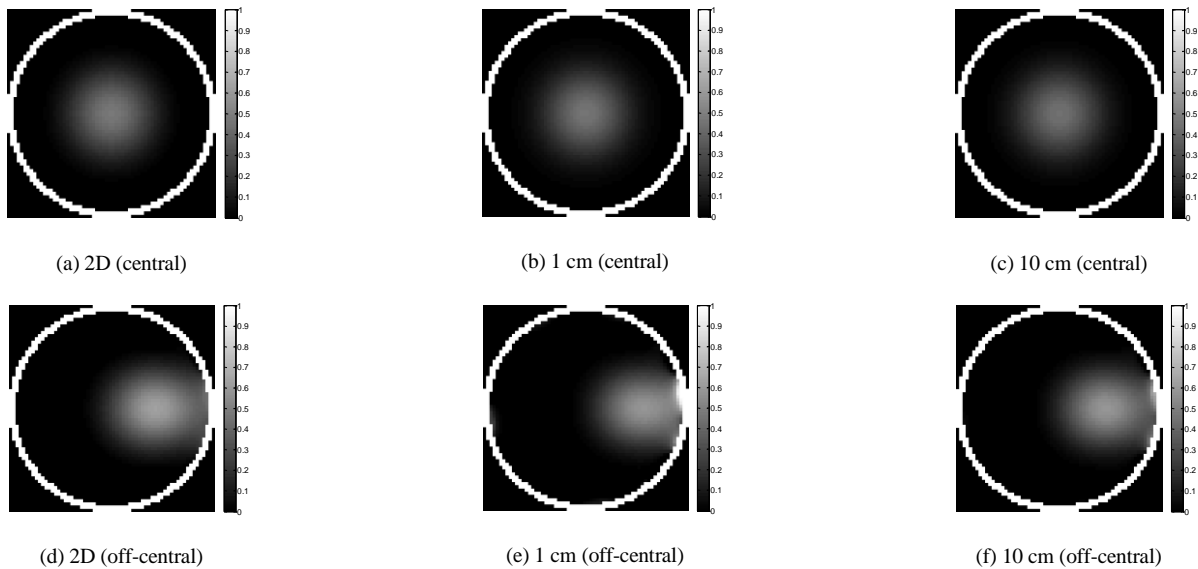(e) 1 cm (off-central)



(f) 10 cm (off-central)

Fig. 14. Reconstruction results for central (a-c) and off-central (d-f) core distribution inside the sensor and with different length after compensation for fringe effect

Another more difficult case is that two objects appear inside and outside the sensor plane at the same time. In this case, the selective scaling should be used to amplify the signal generated by the object inside the sensor plane and remove the unwanted signal induced by the object outside the sensor plane. Given a simple example, a centered non-conductive object with a length of 10 cm is placed inside the sensor plane while a non-centered non-conductive object with a length of 4 cm is positioned above the sensor plane by 3 cm, the cross-sectional and axial view of the two objects are shown in Fig. 15.

With this object setup, the resultant normalized resistances are shown in Fig. 16 (a) together with the 2D reference, the normalized resistances only with the centered non-conductive object of 10 cm inside the sensor plane (identified by "10cm" in Fig. 16 (a) and the same as shown in Fig. 9 (a)) and the normalized resistances only with the non-centered non-conductive object of 4 cm above the sensor plane by 3 cm ("3cm" in Fig. 16 (a) and the same as shown in Fig. 12 (b)). Fig. 16 (a) shows that the resistances with the two objects are distorted due to the fringe effect, compared to those with the object of 10 cm inside the sensor plane. Apparently, the normalized resistance for the 2 objects is superposition of those identified by "10cm" and "3cm" in Fig. 16 (a), but not exactly linear. It is natural to remove the fringe effect induced by the object outside the sensor plane by subtracting the corresponding normalized resistance from the corresponding one for the 2 objects in Fig. 16 (a). By subtraction, scaling is implemented (the scaling factor is the ratio of the maximum normalized resistance in the 2D case to that in this case). The resultant normalized resistance is shown in Fig. 16 (b) together with the 2D reference.
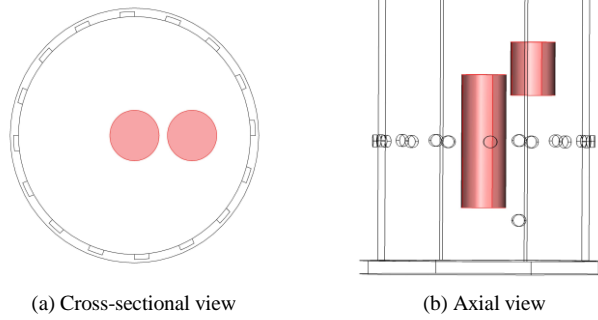
(a) Cross-sectional view　　　　　　　(b) Axial view

Fig. 15. Cross-sectional and axial view of two objects



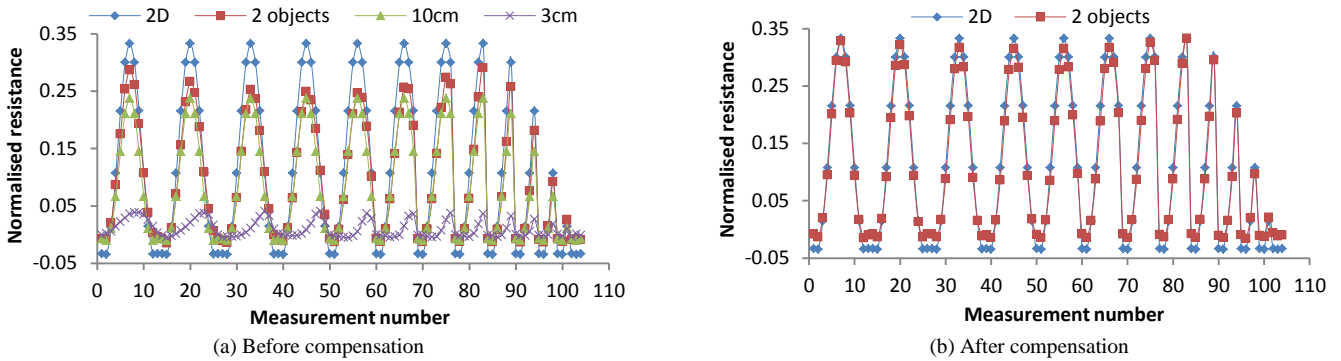(a) Before compensation　　　　　　　(b) After compensation

Fig. 16. Normalized resistances for two objects before and after compensation for fringe effect

Fig. 16 (b) shows that the fringe effect is reduced compared with the corresponding ones in Fig. 16 (a). But small distortion for the normalized resistance still exists because the superposition is not exactly linear. Before the selective scaling, the relative image error corresponding to the normalized resistance for 2 objects in Fig. 16 (a) is about 27%. It is reduced to about 13% with the correlation coefficient around 99.7% after the compensation when the image from the corresponding 2D model is used as the reference. Fig. 17 shows the reconstructed images for two objects before and after compensation for fringe effect referred to the 2D result.



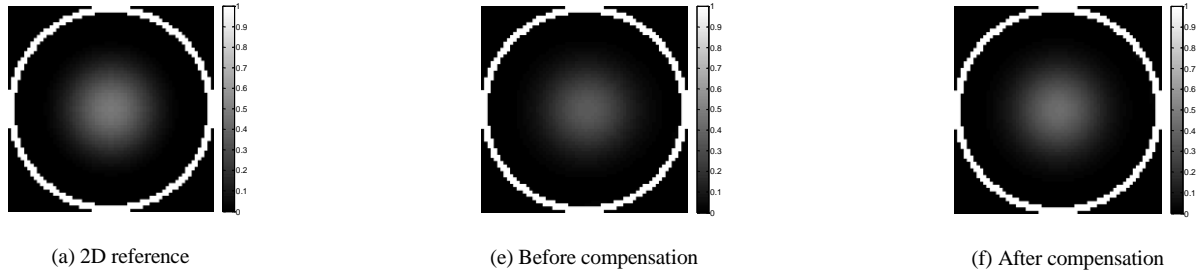(a) 2D reference　　　　　　　(e) Before compensation　　　　　　　(f) After compensation

Fig. 17. Reconstructed images for two objects before and after compensation for fringe effect referred to the 2D result

The above discussion indicates that the selective or direct scaling is effective in reducing the fringe effect. However, to obtain the fringe effect induced by the objects outside the sensor plane, one or two more auxiliary electrode planes are needed. Modeling of the flow patterns in an industrial process to be imaged is also necessary to acquire the 2D references for the related measurements, which is crucial for calculation of the scaling factor. In some complex and extreme circumstances, where the fringe effect overwhelms or distorts the signal too much, it would be difficult to implement this compensation method.

## 4. Experimental verification of findings and proposed methodology

To validate the findings with the single-plane ERT sensor, experiments were carried out. For this purpose, an ERT system was built up, the block diagram of which is shown in Fig. 18:
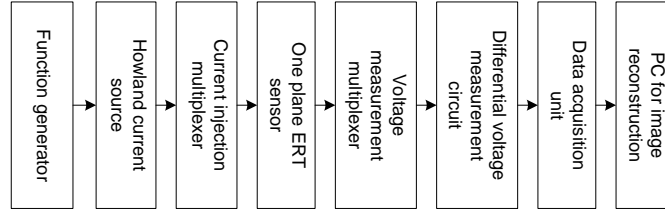
13

Fig. 18. Block diagram of experimental ERT system

As shown in Fig. 18, the experimental ERT system is composed of 7 units: a function generator (HP 33120A), a Howland current source circuit, an ERT sensor, a differential voltage measurement circuit, a current injection and voltage measurement multiplexer module, the function of which is completed manually, a data acquisition unit (Agilent 34972A) and a PC for data acquisition and image reconstruction. In this system, the adjacent current-injection and voltage-measurement strategy is adopted for data acquisition. The function generator is used to drive the Howland current source circuit to output a pair of differential sine-wave currents with almost the same amplitude. By multiplexing, a pair of differential currents is injected into a pair of adjacent electrodes of the ERT sensor. Again by multiplexing, the potential difference between each of possible measurement electrode pairs is conditioned (amplified by 100 times through two stages with each stage 10 times) and then measured by the data acquisition unit. Note that the structure of the differential amplification is the same as the internal structure of PGA202, which is used as the second stage, while the first stage by two OPA602s to enhance the input impedance. Then each measurement is sent to the PC for image reconstruction via an USB interface. Finally an image is reconstructed in MatLab using the data received.

In the experiment, the pair of differential currents has a peak-to-peak magnitude of around 1 mA, and exactly in phase. The frequency of the injected AC current is 10 kHz. Note that the potential difference is also an AC signal and the data acquisition unit (Agilent 34972A) can only measure its root mean square (RMS) value. The amplitude of the AC voltage can be estimated from the measured RMS value by:

$$V_A = V_{RMS} \times Crest\ factor \qquad (9)$$

where $V_A$ is the amplitude of the AC voltage, $V_{RMS}$ is the measured RMS value of the AC voltage, and *Crest factor* is the ratio of the peak value to the RMS value of a waveform, which is calibrated to be 1.414 for the sine wave measured by the data acquisition unit (Agilent Technologies, 2010).

Highly matched resistors are used for the Howland current source circuit (10 K resistors with 0.1% precision and manually matched with each other for a mutual difference less than 0.05%). Together with the high measurement accuracy of Agilent 34972A (maximum 6.5 digits), the measurement accuracy of the experimental system with the above simulation set-ups can be guaranteed. This is confirmed by comparing with corresponding simulation results afterwards. Note that the common mode measurement error was reduced by the relatively high common mode rejection ration (CMRR) of PGA202 (around 70 dB at 10 kHz for a gain of 10) and grounding an unused electrode for reference. Also, high input impedance is guaranteed with the two op-amps OPA602s used in the first stage of differential amplification. The experimental set-up with two objects is shown in Fig. 19 (the PC for image reconstruction is not shown). Note that before starting measurement with Agilent 34972A, a complete self-test was passed (Agilent Technologies, 2010).

To validate the measurement accuracy of the experimental system, experiments were conducted when the tube was filled with the same homogeneous background medium as in the previous simulation, i.e. saline with conductivity of 0.02 S/m. The comparison between the experimental and corresponding 3D simulation results is shown in Fig. 20.

Fig. 20 shows that there is a good agreement between the 3D simulation and experimental results of potential difference with a homogeneous background medium filling the tube. This confirms the measurement accuracy of the above experimental system and partially verifies that the contact impedance has negligible impact on the ERT measurement.

To verify the previous simulation results regarding centered and non-centered distribution inside or outside the sensor plane with non-conductive objects, experiments were carried out with the similar set-ups as shown in Fig. 2 (a) (centered) and Fig. 2 (b) (non-centered) (referring to Fig. 19 (b)). Perspex rods with certain lengths were placed at different axial and horizontal positions during the experiment accordingly. Note that for non-centered distribution, the objects were placed at different horizontal positions from that in Fig. 2 (b). The experimental results of normalized resistance are shown in Fig. 21, where the legends like "4cm" indicate the lengths of the objects for the 3D simulation, "2D" indicates that the result is from the corresponding 2D simulation and those like "4cm(0)" suggest that the object with the specified length is placed outside the sensor plane by the specified distance. Fig. 21 verifies that the same conclusions can be drawn from those experimental results as from the previous corresponding simulation. Apparently, the fringe effect for the objects inside the sensor plane, as shown in Fig. 21 (a) and (b) can be compensated by direct scaling. The following part will focus on the compensation of fringe effect when the distribution with two objects as

shown in Fig. 19 (b) appears inside the tube. The experimental results of normalized resistance are shown in Fig. 22 together with related 2D simulation and experimental results including that after compensation by selective scaling.
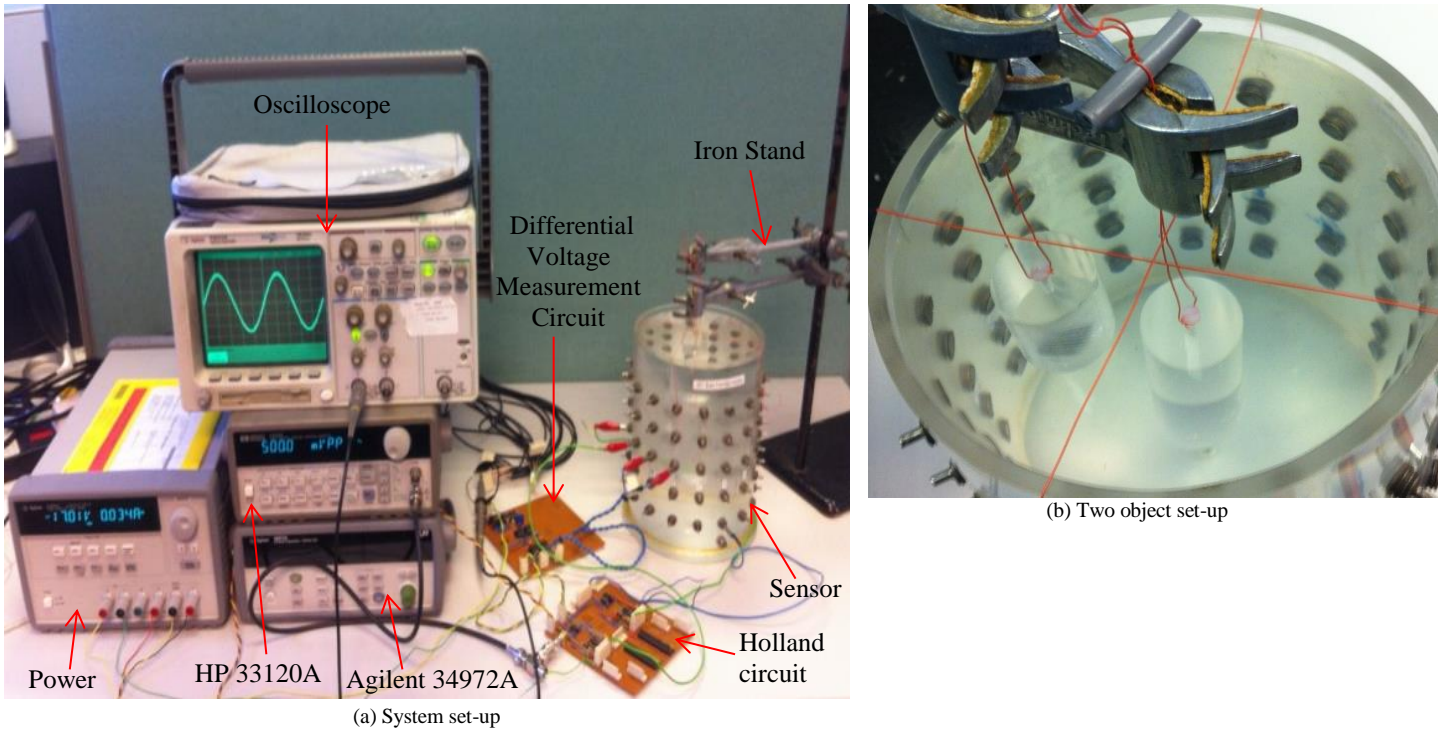


(a) System set-up



(b) Two object set-up
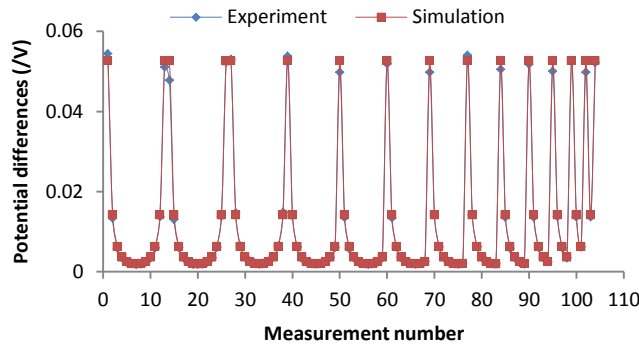
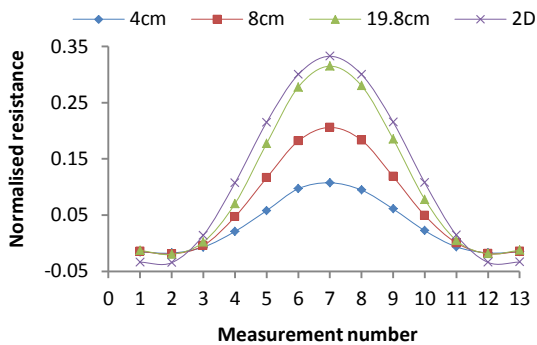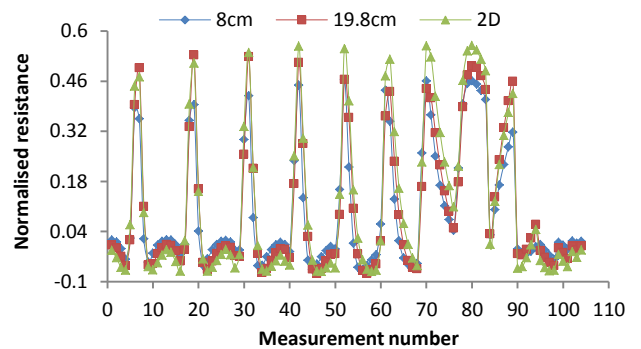Fig. 19. Experimental set-up with two objects



Fig. 20. Comparison between 3D simulation and experimental results of potential difference with homogeneous background medium filling the tube
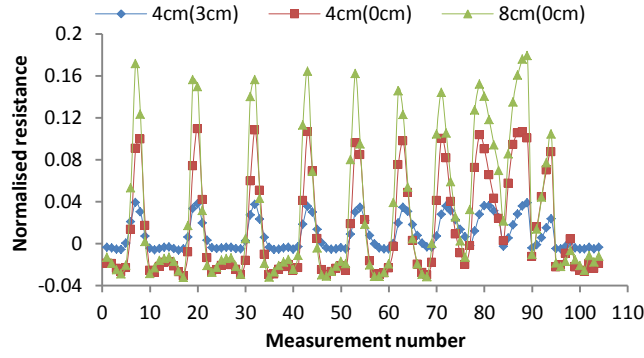


(a) Centered distribution inside the sensor plane



(b) Non-centered distribution inside the sensor plane

(c) Non-centered distribution outside the sensor plane

Fig. 21. Experimental results of normalized resistance for centered and non-centered non-conductive objects inside or outside the sensor plane

In Fig. 22, the legend "2 objects" represents the experimental result for the two objects. "8cm(core)" for the centered object with a length of 8 cm. "Compensated" indicates the normalized resistance after compensation for fringe effect. Other legends have the same meanings as before. Note that the centered object ("8cm(core)") is not axially symmetric to the sensor plane but a little upward (by 1 cm), which explains why the normalized resistance in this case is a little different from that in Fig. 21 (a). Fig. 22 also shows that there is less fringe effect in the normalized resistance after compensation by selective scaling. This is consistent with the conclusions drawn from the previous simulation.
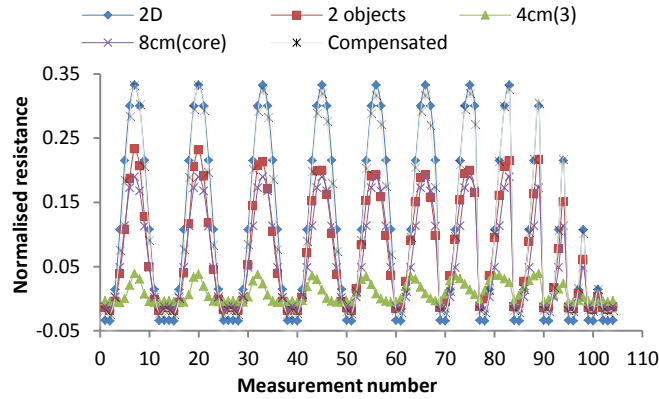


Fig. 22. Experimental results of normalized resistance for the distribution with two objects and related 2D simulation or experimental results including the one after compensation

The above experimental results confirm that the previous 3D simulation results are valid, and verify the feasibility of the proposed methodology for the reduction of the fringe effect. It is promising to use the direct or selective scaling to compensate for the fringe effect, but difficulties still need to be addressed, e.g. the determination of the scaling factor by calibration and the more complicated distribution to be imaged.

## 5. Conclusions

The objective of this study was to evaluate the fringe effect with a single-plane ERT sensor for some simple but typical distributions, e.g. centered or non-centered and inside or outside the sensor plane, which are also variable in axial length and not axially homogeneous in most cases. Our goal was to illustrate to what extent an ERT sensor is affected by the fringe effect in these situations and try to draw some generalized conclusions, which may be used for compensation of the fringe effect. A 3D simulation model was established, and experiments were conducted to validate this model and the conclusions drawn from the related simulation results as well as the methodology proposed for compensation of the fringe effect.

Initially, the difference between ERT and ECT was analyzed to explain why an ERT sensor with pin electrodes has negligible fringe effect for an axially homogeneous distribution. This explanation was further confirmed by the corresponding simulation. For non-axially homogeneous distributions inside the sensor discussed in this study, i.e. centered or non-centered single object with a length shorter than that of the tube, less fringe effect would occur with longer objects while the relationship curve of the normalized resistance with measurement number is of the similar shape to the 2D one in all the cases. For a single non-conductive object outside the sensor plane, either centered or non-centered, its induced fringe effect would decrease with its distance from the sensor

16

plane for the same axial length, but increase with its axial length for the same distance. For two non-conductive objects, one centered and inside the sensor plane while the other non-centered and outside the sensor plane, the resultant resistance after normalization is the superposition of the normalized resistance when each object appears separately.

In view of the above conclusions, a compensation method for the fringe effect was proposed, i.e. selective scaling of the normalized resistance regarding the corresponding 2D reference. Both simulation and experiment proved the feasibility of the method using a simple setup with two objects. Further work needs to be dedicated to the design of ERT sensors with one or two auxiliary electrode planes, which would help sense the fringe effect induced by the objects outside the sensor plane.

## Acknowledgment

## References

[1]   Agilent Technologies (2010), Agilent 34970A/34972A data acquisition/switch unit user's guide, Second Edition, Printed in Malaysia.

[2]   Banasiak R, Wajman R, Sankowski D, and Soleimani M (2010), "Three-dimensional nonlinear inversion of electrical capacitance tomography data using a complete sensor model," Progress In Electromagnetics Research, vol. 100, pp. 219–234.

[3]   Banasiak R, Ye Z, and Soleimani M (2012), "Improving three-dimensional electrical capacitance tomography imaging using approximation error model theory," Journal of Electromagnetic Waves and Applications, vol. 26:2-3, pp. 411–421.

[4]   Cao Z, and Xu L J (2013), "Direct image reconstruction for 3-D electrical resistance tomography by using the factorization method and electrodes on a single plane," IEEE Trans. on Inst. and Meas., vol. 62, pp. 999–1007.

[5]   Dehghani H, Soni N, Halter R, Hartov A, and Paulsen K D  (2005), "Excitation patterns in three-dimensional electrical impedance tomography," Physiol. Meas., vol. 26, pp. S185–S197.

[6]   Dickin F, and Wang M (1996), "Electrical resistance tomography for process applications," Meas. Sci. Technol., vol. 7, pp. 247–260.

[7]   Fransolet E, Crine M, Homme G L, Toye D, and Marchot P (2001), "Analysis of electrical resistance tomography measurements obtained on a bubble column," Meas. Sci. Technol., vol. 12, pp. 1055–1060.

[8]   Fransolet E, Crine M, Homme G L, Toye D, and Marchot P (2002), "Electrical resistance tomography sensor simulations: comparison with experiments," Meas. Sci. Technol., vol. 13, pp. 1239–1247.

[9]   Fransolet E, Crine M, Marchot P, and Toye D (2005), "Analysis of gas holdup in bubble columns with non-Newtonian fluid using electrical resistance tomography and dynamic gas disengagement technique," Chem. Eng. Sci., vol. 60, pp. 6118–6123.

[10]  Giguère R, Fradette L, Mignon D, and Tanguy P A (2008), "ERT algorithms for quantitative concentration measurement of multiphase flows," Chem. Eng. J., vol. 141, pp. 305–317.

[11]  Jin H, Wang M, and Williams R A (2007), "Analysis of bubble behaviors in bubble columns using electrical resistance tomography," Chem. Eng. J., vol. 130, pp. 179–185.

[12]  Li Y (2008), Key issues of 2D/3D image reconstruction in electrical tomography, PhD thesis, The University of Manchester, UK.

[13]  Li Y, and Yang W Q (2009), "Measurement of multi-phase distribution using an integrated dual-modality sensor," Proc. IEEE Int. Workshop on Imaging Systems and Techniques (Shenzhen, China, May 2009), pp. 335–339.

[14]  Lionheart W R B (2001), "Reconstruction Algorithms for Permittivity and Conductivity Imaging," Proc. of the 2nd World Congress on Industrial Process Tomography (Hannover, Germany, August 2001), pp. 4–11.

[15]  Ma Y X, Wang H, Xu L A, and Jiang C Z (1997), "Simulation study of the electrode array used in an ERT system," Chem. Eng. Sci., vol. 52, pp. 2197–2203.

[16]  Marashdeh Q, Fan L -S, Du B, and Warsito W (2008), "Electrical capacitance tomography-a perspective," Ind. Eng. Chem. Res., vol. 47, pp. 3708–3719.

[17]  Murphy S C, Stanley S J, Rhodes D, and York T A (2006), "3D electrical tomographic imaging using vertical arrays of electrodes," Meas. Sci. Technol., vol. 17, pp. 3053–3065.

[18]  Neumayer M, Zangl H, Watzenig D, and Fuchs A (2011), "Current reconstruction algorithms in electrical capacitance tomography," in New Developments and Applications in Sensing Technology, vol. 83. Berlin, Germany: Springer-Verlag, ser. Lecture Notes in Electrical Engineering, pp. 65–106.

[19]  Pinheiro P A T, Loh W W, and Dickin F J (1998), "Three-dimensional reconstruction algorithm for electrical resistance tomography," IEE Proc.-Sci. Meas. Technol., vol. 145, pp. 85–93.

[20]  Rabbani K S, and Kabir A M B H (1991), "Studies on the effect of the third dimension on a two-dimensional electrical impedance tomography system," Clin. Phys. Physiol. Meas., vol. 12, pp. 393–402.

[21]  Soleimani M, Mitchell C N, Banasiak R, Wajman R, and Adler A (2009), "Four-dimensional electrical capacitance tomography imaging using experimental data," Progress In Electromagnetics Research, vol. 90, pp. 171–186.

[22]  Soleimani M, Wang H G, Li Y, and Yang W Q (2007), "A comparative study of 3d electrical capacitance tomography," Int. J. of Inf. and Sys. Sci., vol. 3, pp. 292–306.

[23]  Sun J T, and Yang W Q (2013), "Fringe effect of electrical capacitance and resistance tomography sensors," Meas. Sci. Technol., vol. 24, 074002 (15pp).

[24] Szczepanik Z, and Rucki Z (2007), "Field analysis and electrical models of multi-electrode impedance sensors," Sensors and Actuators: A, vol. 133, pp. 13–22.

[25] Toye D, Fransolet E, Simon D, Crine M, L'Homme G, and Marchot P (2005), "Possibilities and limits of application of electrical resistance tomography in hydrodynamics of bubble columns," Can. J. Chem. Eng., vol. 83, pp. 4–10.

[26] Vijayan M, Schlaberg H I, and Wang M (2007), "Effects of Sparger geometry on the mechanism of flow pattern transition in a bubble column," Chem. Eng. J., vol. 130, pp. 171–178.

[27] Wang M (1999), "Three-dimensional effects in electrical impedance tomography," Proc. 1st World Congress on Industrial Process Tomography (Buxton, UK, April 1999), pp 410–415.

[28] Warsito W, and Fan L -S(2005), "Dynamics of spiral bubble plume motion in the entrance region of bubble columns and three-phase fluidized beds using 3D ECT," Chem. Eng. Sci., vol. 60, pp. 6073–6084.

[29] Wilkinson A J, Randall E W, Long T M, and Collins A (2006), "The design of an ERT system for 3D data acquisition and a quantitative evaluation of its performance," Meas. Sci. Technol., vol. 17, pp. 2088–2096.

[30] Yang W Q, and Peng L H (2003), "Image reconstruction algorithms for electrical capacitance tomography," Meas. Sci. Technol., vol. 14, pp. R1–R13.